



102-nm, 44.5-MHz inertial-free swept source by mode-locked fiber laser and time stretch technique for optical coherence tomography

JIQIANG KANG, PINGPING FENG, XIAOMING WEI, EDMUND Y. LAM, KEVIN K. TSIA, AND KENNETH K. Y. WONG*

Department of Electrical and Electronic Engineering, The University of Hong Kong, Pokfulam Road, Hong Kong, China

*kywong@eee.hku.hk

Abstract: A swept source with both high repetition-rate and broad bandwidth is indispensable to enable optical coherence tomography (OCT) with high imaging rate and high axial resolution. However, available swept sources are commonly either limited in speed (sub-MHz) by inertial or kinetic component, or limited in bandwidth (<100 nm) by the gain medium. Here we report an ultrafast broadband (over 100 nm centered at 1.55- μm) all-fiber inertial-free swept source built upon a high-power dispersion-managed fiber laser in conjunction with an optical time-stretch module which bypasses complex optical amplification scheme, which result in a portable and compact implementation of time-stretch OCT (TS-OCT) at A-scan rate of 44.5-MHz, axial resolution of 14 μm in air (or 10 μm in tissue), and flat sensitivity roll-off within 4.3 mm imaging range. Together with the demonstration of two- and three-dimensional OCT imaging of a mud-fish eye anterior segment, we also perform comprehensive studies on the imaging depth, receiver bandwidth, and group velocity dispersion condition. This all-fiber inertia-free swept source could provide a promising source solution for SS-OCT system to realize high-performance volumetric OCT imaging in real time.

© 2018 Optical Society of America under the terms of the [OSA Open Access Publishing Agreement](#)

OCIS codes: (140.3500) Lasers, erbium; (140.4050) Mode-locked lasers; (110.4500) Optical coherence tomography; (120.3180) Interferometry.

References and links

1. D. Huang, E. A. Swanson, C. P. Lin, J. S. Schuman, W. G. Stinson, W. Chang, M. R. Hee, T. Flotte, K. Gregory, C. A. Puliafito, and J. G. Fujimoto, "Optical Coherence Tomography," *Science* **254**(5035), 1178–1181 (1991).
2. W. Drexler and J. G. Fujimoto, *Optical Coherence Tomography: Technology and Application*, 2nd ed. (Springer, 2008).
3. J. S. Schuman, C. A. Puliafito, J. G. Fujimoto, and J. S. Duker, eds., *Optical Coherence Tomography of Ocular Diseases*, 3rd ed. (Slack Inc., 2004).
4. H. Yabushita, B. E. Bouma, S. L. Houser, H. T. Aretz, I. K. Jang, K. H. Schlendorf, C. R. Kauffman, M. Shishkov, D. H. Kang, E. F. Halpern, and G. J. Tearney, "Characterization of Human Atherosclerosis by Optical Coherence Tomography," *Circulation* **106**(13), 1640–1645 (2002).
5. Y. Yoon, W. H. Jang, P. Xiao, B. Kim, T. Wang, Q. Li, J. Y. Lee, E. Chung, and K. H. Kim, "In vivo wide-field reflectance/fluorescence imaging and polarization-sensitive optical coherence tomography of human oral cavity with a forward-viewing probe," *Biomed. Opt. Express* **6**(2), 524–535 (2015).
6. M. Choma, M. Sarunic, C. Yang, and J. Izatt, "Sensitivity advantage of swept source and Fourier domain optical coherence tomography," *Opt. Express* **11**(18), 2183–2189 (2003).
7. R. Leitgeb, C. Hitzenberger, and A. Fercher, "Performance of fourier domain vs. time domain optical coherence tomography," *Opt. Express* **11**(8), 889–894 (2003).
8. Y. Watanabe, F. Sajima, T. Itagaki, K. Watanabe, and Y. Shuto, "High-speed linear detection time domain optical coherence tomography with reflective grating-generated spatial reference delay," *Appl. Opt.* **48**(18), 3401–3406 (2009).
9. R. I. Macdonald, "Frequency domain optical reflectometer," *Appl. Opt.* **20**(10), 1840–1844 (1981).
10. T. Bajraszewski, M. Wojtkowski, M. Szkulmowski, A. Szkulmowska, R. Huber, and A. Kowalczyk, "Improved spectral optical coherence tomography using optical frequency comb," *Opt. Express* **16**(6), 4163–4176 (2008).
11. T. H. Tsai, C. Zhou, D. C. Adler, and J. G. Fujimoto, "Frequency comb swept lasers," *Opt. Express* **17**(23), 21257–21270 (2009).

12. T. Klein, W. Wieser, L. Reznicek, A. Neubauer, A. Kampik, and R. Huber, "Multi-MHz retinal OCT," *Biomed. Opt. Express* **4**(10), 1890–1908 (2013).
13. W. Y. Oh, B. J. Vakoc, M. Shishkov, G. J. Tearney, and B. E. Bouma, ">400 kHz repetition rate wavelength-swept laser and application to high-speed optical frequency domain imaging," *Opt. Lett.* **35**(17), 2919–2921 (2010).
14. B. D. Goldberg, S. M. Motaghian Nezam, P. Jillella, B. E. Bouma, and G. J. Tearney, "Miniature swept source for point of care optical frequency domain imaging," *Opt. Express* **17**(5), 3619–3629 (2009).
15. R. Huber, M. Wojtkowski, and J. G. Fujimoto, "Fourier Domain Mode Locking (FDML): A new laser operating regime and applications for optical coherence tomography," *Opt. Express* **14**(8), 3225–3237 (2006).
16. D. C. Adler, Y. Chen, R. Huber, J. Schmitt, J. Connolly, and J. G. Fujimoto, "Three-dimensional endomicroscopy using optical coherence tomography," *Nat. Photonics* **1**(12), 709–716 (2007).
17. E. C. Vail, G. S. Li, W. Yuen, and C. J. Chang-Hasnain, "High performance micromechanical tunable vertical cavity surface emitting lasers," *Electron. Lett.* **32**(20), 1888–1889 (1996).
18. Z. Wang, B. Potsaid, L. Chen, C. Doerr, H.-C. Lee, T. Nielson, V. Jayaraman, A. E. Cable, E. Swanson, and J. G. Fujimoto, "Cubic meter volume optical coherence tomography," *Optica* **3**(12), 1496–1503 (2016).
19. I. Grulkowski, J. J. Liu, B. Potsaid, V. Jayaraman, C. D. Lu, J. Jiang, A. E. Cable, J. S. Duker, and J. G. Fujimoto, "Retinal, anterior segment and full eye imaging using ultrahigh speed swept source OCT with vertical-cavity surface emitting lasers," *Biomed. Opt. Express* **3**(11), 2733–2751 (2012).
20. T. Klein and R. Huber, "High-speed OCT light sources and systems [Invited]," *Biomed. Opt. Express* **8**(2), 828–859 (2017).
21. R. Huber, D. C. Adler, and J. G. Fujimoto, "Buffered Fourier domain mode locking: Unidirectional swept laser sources for optical coherence tomography imaging at 370,000 lines/s," *Opt. Lett.* **31**(20), 2975–2977 (2006).
22. C. Jun, M. Villiger, W. Y. Oh, and B. E. Bouma, "All-fiber wavelength swept ring laser based on Fabry-Perot filter for optical frequency domain imaging," *Opt. Express* **22**(21), 25805–25814 (2014).
23. W. Wieser, B. R. Biedermann, T. Klein, C. M. Eigenwillig, and R. Huber, "Multi-Megahertz OCT: High quality 3D imaging at 20 million A-scans and 4.5 GVoxels per second," *Opt. Express* **18**(14), 14685–14704 (2010).
24. J. P. Kolb, T. Pfeiffer, M. Eibl, H. Hakert, and R. Huber, "High-resolution retinal swept source optical coherence tomography with an ultra-wideband Fourier-domain mode-locked laser at MHz A-scan rates," *Biomed. Opt. Express* **9**(1), 120–130 (2017).
25. M. Bonesi, M. P. Minneman, J. Ensher, B. Zabihian, H. Sattmann, P. Boschert, E. Hoover, R. A. Leitgeb, M. Crawford, and W. Drexler, "Akinetic all-semiconductor programmable swept-source at 1550 nm and 1310 nm with centimeters coherence length," *Opt. Express* **22**(3), 2632–2655 (2014).
26. M. P. Minneman, J. Ensher, M. Crawford, and D. Derickson, "All-semiconductor high-speed akinetic swept-source for OCT," In *Asia Communications and Photonics* (SPIE-OSA-IEEE, 2011), **8311**, 831116.
27. J. Xu, S. Song, W. Wei, and R. K. Wang, "Wide field and highly sensitive angiography based on optical coherence tomography with akinetic swept source," *Biomed. Opt. Express* **8**(1), 420–435 (2016).
28. S. Song, J. Xu, and R. K. Wang, "Long-range and wide field of view optical coherence tomography for *in vivo* 3D imaging of large volume object based on akinetic programmable swept source," *Biomed. Opt. Express* **7**(11), 4734–4748 (2016).
29. J. Xu, C. Zhang, J. Xu, K. K. Y. Wong, and K. K. Tsia, "Megahertz all-optical swept-source optical coherence tomography based on broadband amplified optical time-stretch," *Opt. Lett.* **39**(3), 622–625 (2014).
30. J. Xu, X. Wei, L. Yu, C. Zhang, J. Xu, K. K. Y. Wong, and K. K. Tsia, "Performance of megahertz amplified optical time-stretch optical coherence tomography (AOT-OCT)," *Opt. Express* **22**(19), 22498–22512 (2014).
31. J. Xu, X. Wei, L. Yu, C. Zhang, J. Xu, K. K. Y. Wong, and K. K. Tsia, "High-performance multi-megahertz optical coherence tomography based on amplified optical time-stretch," *Biomed. Opt. Express* **6**(4), 1340–1350 (2015).
32. K. Goda, D. R. Solli, and B. Jalali, "Real-time optical reflectometry enabled by amplified dispersive Fourier transformation," *Appl. Phys. Lett.* **93**(3), 031106 (2008).
33. K. Goda, K. K. Tsia, and B. Jalali, "Serial time-encoded amplified imaging for real-time observation of fast dynamic phenomena," *Nature* **458**(7242), 1145–1149 (2009).
34. Y. Zhou, K. K. H. Chan, T. Lai, and S. Tang, "Characterizing refractive index and thickness of biological tissues using combined multiphoton microscopy and optical coherence tomography," *Biomed. Opt. Express* **4**(1), 38–50 (2013).
35. L. M. Zhao, D. Y. Tang, and J. Wu, "Gain-guided soliton in a positive group-dispersion fiber laser," *Opt. Lett.* **31**(12), 1788–1790 (2006).
36. P. Grelu and N. Akhmediev, "Dissipative soliton for mode-locked lasers," *Nat. Photonics* **6**(2), 84–92 (2012).
37. L. E. Nelson, D. J. Jones, K. Tamura, H. A. Haus, and E. P. Ippen, "Ultrashort-pulse fiber ring lasers," *Appl. Phys. B* **65**(2), 277–294 (1997).
38. L. M. Zhao, D. Y. Tang, H. Zhang, T. H. Cheng, H. Y. Tam, and C. Lu, "Dynamics of gain-guided solitons in an all-normal-dispersion fiber laser," *Opt. Lett.* **32**(13), 1806–1808 (2007).
39. X. Wei, J. Xu, Y. Xu, L. Yu, J. Xu, B. Li, A. K. S. Lau, X. Wang, C. Zhang, K. K. Tsia, and K. K. Y. Wong, "Breathing laser as an inertia-free swept source for high-quality ultrafast optical bioimaging," *Opt. Lett.* **39**(23), 6593–6596 (2014).
40. R. Steiner, "Laser-Tissue Interactions," in *Laser and IPL Technology in Dermatology and Aesthetic Medicine*, C. Raulin and S. Karsai, eds. (Springer, 2011), pp. 23–36.

41. B. E. Bouma, L. E. Nelson, G. J. Tearney, D. J. Jones, M. E. Brezinski, and J. G. Fujimoto, "Optical coherence tomographic imaging of human tissue at 1.55 μm and 1.81 μm using Er-and Tm-doped fiber sources," *J. Biomed. Opt.* **3**(1), 76–79 (1998).
42. X. Wei, S. Xu, H. Huang, M. Peng, and Z. Yang, "Compact all-fiber ring femtosecond laser with high fundamental repetition rate," *Opt. Express* **20**(22), 24607–24613 (2012).
43. C. D. Lu, M. F. Kraus, B. Potsaid, J. J. Liu, W. Choi, V. Jayaraman, A. E. Cable, J. Hornegger, J. S. Duker, and J. G. Fujimoto, "Handheld ultrahigh speed swept source optical coherence tomography instrument using a MEMS scanning mirror," *Biomed. Opt. Express* **5**(1), 293–311 (2013).
44. X. Yu, X. Liu, S. Chen, Y. Luo, X. Wang, and L. Liu, "High-resolution extended source optical coherence tomography," *Opt. Express* **23**(20), 26399–26413 (2015).
45. J. Ke and E. Y. Lam, "Image reconstruction from nonuniformly spaced samples in spectral-domain optical coherence tomography," *Biomed. Opt. Express* **3**(4), 741–752 (2012).
46. J. Gong, B. Liu, Y. L. Kim, Y. Liu, X. Li, and V. Backman, "Optimal spectral reshaping for resolution improvement in optical coherence tomography," *Opt. Express* **14**(13), 5909–5915 (2006).
47. R. Huber, M. Wojtkowski, K. Taira, J. Fujimoto, and K. Hsu, "Amplified, frequency swept lasers for frequency domain reflectometry and OCT imaging: design and scaling principles," *Opt. Express* **13**(9), 3513–3528 (2005).
48. J. Kang, X. Wei, B. Li, X. Wang, L. Yu, S. Tan, C. Jinata, and K. K. Y. Wong, "Sensitivity enhancement in swept-source optical coherence tomography by parametric balanced detector and amplifier," *Biomed. Opt. Express* **7**(4), 1294–1304 (2016).
49. A. N. S. Institute, "American national standard for safe use of lasers," ANSI Z136.1–200 (2000).
50. J. Image, <https://imagej.nih.gov/ij/>.
51. W. Wieser, W. Draxinger, T. Klein, S. Karpf, T. Pfeiffer, and R. Huber, "High definition live 3D-OCT in vivo: design and evaluation of a 4D OCT engine with 1 GVoxel/s," *Biomed. Opt. Express* **5**(9), 2963–2977 (2014).
52. A. E. Desjardins, B. J. Vakoc, M. J. Suter, S. H. Yun, G. J. Tearney, and B. E. Bouma, "Real-Time FPGA Processing for High-Speed Optical Frequency Domain Imaging," *IEEE Trans. Med. Imaging* **28**(9), 1468–1472 (2009).

1. Introduction

Optical coherence tomography (OCT) is a well-recognized non-contact and non-invasive cross-sectional imaging modality for two-dimensional (2D) and three-dimensional (3D) tissue architecture visualization [1]. Akin to B-mode ultrasound, OCT detects the echo time delay as well as the intensity of the reflected or backscattered light from deep tissue structures in an axial scan (A-scan) by means of optical interference. Thousands of A-scan lines are formatted into 2D or 3D images through light beam scanning [2]. The label-free and deep-tissue (>1mm) imaging capability of OCT renders it very favorable in a wide range of clinical applications in ophthalmology [3], intravascular plaque assessment [4], and dentistry [5], etc.

Swept source OCT (SS-OCT) is an important member in nowadays OCT family. Comparing with time-domain OCT (TD-OCT), SS-OCT features with much higher imaging speed and high detection sensitivity [6–8], while comparing with spectrum-domain OCT (SD-OCT), SS-OCT has faster imaging speed and flatten sensitivity roll-off versus imaging depth [9–11]. High speed and high resolution SS-OCT renders volumetric structural and functional tissue imaging in real-time more promising [12]. SS-OCT generally consists of three modules, i.e. a broadband narrow linewidth frequency rapidly swept optical source, an interferometer with light scanning mechanism, and an interferometric signal detection and processing unit. The interference signal is detected as a function of time when the optical frequency is rapidly swept, and a balanced detector (BD) together with a broadband analog-to-digital converter (ADC) are normally used. Therefore, the imaging speed at SS-OCT, i.e. A-scan rate, is thus determined by the repetition rate of the swept source, light scanning speed on sample, and signal processing speed. Moreover, the instantaneous linewidth of the swept source and the bandwidth of the ADC determines the spectral resolution, and high spectral resolution enables the reduction of sensitivity roll-off in SS-OCT and thus extends the imaging depth. For these practical demands, a high-performance swept source with fast repetition rate, broad bandwidth, and narrow linewidth have attracted spectacular attention in recent years for a practical SS-OCT system.

Currently, a diversity of swept sources are proposed and developed for SS-OCT, such as the external cavity tunable lasers with rotating or scanning mirror [13,14], Fourier domain mode locking (FDML) lasers with Fabry-Pérot cavity [15,16], and short-cavity

microelectromechanical systems (MEMS) tunable lasers [17,18], etc. The performance of these swept sources are well reviewed in [19,20]. However, those swept sources are either limited in speed at sub-MHz level by the inertial or kinetic component inside the optical source for its intrinsic momentum-induced limitations in scanning speed, or limited in bandwidth to less than 100 nm by the gain medium. Although multi-MHz sweep rates is achievable with buffering technologies [21–24], the setup will be slightly complicated. Consequently, it is essential to explore broadband inertia-free optical swept sources for SS-OCT.

For this purpose, a type of all-semiconductor akinetic swept source was developed recently [25]. This swept source is a monolithic semiconductor device without moving parts and its frequency tuning is realized by modulating the refraction index to change the cavity length and spacing of the distributed Bragg grating by an electrical signal [26]. This novel source features with small size, single longitudinal mode operation, and 100-nm optical bandwidth, which make it a promising solution for high performance OCT application [27,28]. However, its hundreds of kHz sweep rate has large room for improvement to achieve MHz-level imaging speed. On the other hand, another type of inertia-free swept source by leveraging stable mode-locked fiber laser and amplified optical time-stretch has recently been proposed, i.e. AOT-OCT [29–31]. AOT-OCT shows its promises in realizing high-performance volumetric OCT imaging at video rate for its multi-MHz repetition rate. The performance of the swept source relies on the performance of fiber laser, such as the optical bandwidth, repetition rate, and output power. In previous work, the swept rate was more than 10 MHz, but the optical bandwidth is only 56 nm centered at 1558 nm. Narrow optical bandwidth limits the axial resolution in AOT-OCT. Besides, its direct output power was relatively low, ~2 mW, and thus a complicated fiber Raman amplifier should be implemented in the time-stretch stage to boost optical power and improve imaging sensitivity [32,33]. To further improve the performance of such type of all-fiber inertia-free swept source, a much broader band high power fiber laser is highly demanded. In addition, a broadband high power fiber laser will also be useful to construct hybrid optical imaging system by combing OCT and nonlinear imaging [34].

In practice, it was demonstrated that stable mode-locked pulses could be generated in dispersion-managed fiber lasers by tailoring the intracavity dispersion properly, i.e., near zero but net-normal dispersion regime [35–37]. Different from conventional soliton which is susceptible to pulse splitting for soliton energy quantization effect, dispersion-managed pulses can resist optical wave breaking effect to a certain extent and thus it can realize high-power operation [38]. Besides, the rectangular-like spectral profile of the dispersion-managed pulses can improve the effective optical bandwidth making it suitable for the practical application where broad bandwidth is highly demanded [39]. For these reasons, dispersion-managed fiber laser is a good choice for obtaining broadband high-power mode-locked pulses.

In this paper, we demonstrate an all-fiber swept source by leveraging dispersion-managed fiber laser and time-stretch technique. The erbium-doped fiber (EDF) laser has 102-nm 10-dB optical bandwidth centered at 1.55- μm , 22-mW direct output average power, and 1.6-ps pulse width at 44.5-MHz repetition rate. This source considerably outperforms the work presented in [29–31]. The >100 nm optical bandwidth is comparable with conventional inertia-based swept source with semiconductor optical amplifiers (SOA), e.g. FDML laser, but the repetition rate is more than two orders of magnitude higher without buffering stages. In the time-stretch part, a spool of 11.9-km single-mode fiber (SMF) was used to chirp the direct output pulses to realize a swept source through frequency/wavelength to time mapping. Taking advantage of this fiber laser's relative high output power, fiber Raman amplification in time-stretch part is no longer necessary. This significantly simplifies the system configuration and thus favors practical ultrafast OCT applications. Therefore, the OCT system incorporating this swept source is denoted as time-stretch OCT (TS-OCT) here for

simplicity. By using a high performance BD, the proposed TS-OCT has axial resolution of 14 μm in air corresponding to 10 μm in tissue (with $n = 1.4$ [40]), and flat sensitivity roll-off within 4.3 mm imaging range. Two-dimensional (2D) and three-dimensional (3D) OCT imaging with a mud-fish eye anterior segment was conducted to verify the imaging capability of our TS-OCT system. It is worthy to note that, a dispersion-managed fiber lasers with bandwidth of 80 nm center at 1.55- μm was successfully applied in TD-OCT [41], and it is the first time that an EDF laser with larger than 100 nm bandwidth was realized and used in SS-OCT, to the best of our knowledge. This all-fiber inertia-free swept source provides a promising solution for SS-OCT system to realize high-performance volumetric OCT imaging in real time.

2. Experimental setup

The schematic diagram of the proposed TS-OCT is shown in Fig. 1, which comprises of a swept source, a Michelson interferometer with a 1D/2D-scanning galvo mirror, and an interferometric signal detection and processing unit.

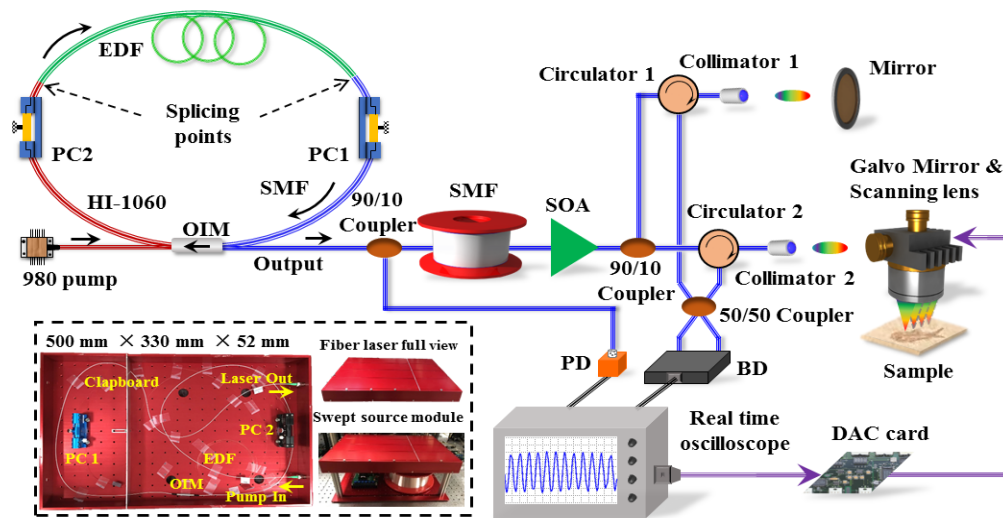


Fig. 1. Schematic diagram of the proposed TS-OCT system. **OIM**: optical integrated module; **EDF**: erbium-doped fiber; **PC**, polarization controller; **SMF**: standard single-mode fiber; **SOA**: amplified spontaneous emission; **PD**: photodetector; **BD**: balanced detector; **DAC**: digital-to-analog converter.

The fiber laser was a dispersion-managed fiber ring laser mode-locked by nonlinear polarization rotation (NPR) technique. The cavity consisted of three sections of SMF, i.e., 0.5-m HI-1060 fiber (Corning, HI 1060) in red color, 3.6-m lowly-doped EDF (Lucent-SFD) in green color, and 0.5-m standard SMF (Corning, SMF 28e) in blue color. The total cavity dispersion is 0.03 ps^2 . The EDF was core-pumped by a 976-nm single-mode laser diode (LD). Both pump coupling and lasing signal extraction were realized by a single unit in a reflection mode, i.e., a single-mode optical integrated module (OIM) incorporating wavelength-division multiplexing (WDM), beam splitter, and polarization-sensitive isolator. The beam splitter inside the OIM extracted 50% optical signal from the fiber cavity. More details about this OIM have been covered in [42]. Two in-line polarization controllers (PCs) were inserted into the cavity to manipulate the polarization state of the light. Broadband operation can be realized by the composite operation of nonlinearity (mainly the self-phase modulations), dispersion, and polarization [37]. The direct output average power was 22 mW with 112 mW pump power. The direct output power was splitted by a 90/10 coupler, and the 10% power was used as the trigger signal for the real-time oscilloscope, while the pulses with remaining

90% power was chirped by a spool of 11.9-km SMF corresponding to a total GVD of 0.2 ns/nm. The loss of the time-stretch part was 4.5 dB, and the power after that was 5 mW. Eventually, the fiber laser was housed into a customized aluminum chamber (500 mm × 330 mm × 52 mm) to isolate the environmental perturbations, e.g., mechanical vibration and temperature change, which thus enables portable and robust operations, as shown in the dashed box in Fig. 1. The 11.9-km SMF was integrated with the fiber laser into a swept-source module for portable and compact operation.

A C-band SOA (Covega SOA-1140) was used to boost the power and reshape the optical spectrum after the time-stretch part. The maximum amplified power after the SOA was 20 mW (13 dBm) limited by the saturation power of the SOA. The amplified and reshaped pulse train was afterwards launched into the Michelson interferometer. Another 90/10 coupler was used to split 10% of the input power into reference arm, and 90% into sample arm. A scanning lens (LSM03, Thorlabs) with 36-mm effective focal length and 4 mm aperture size was used after the galvo mirror to focus the light beam on the sample, while a dispersion compensator (LSM03DC, Thorlabs) was used to compensate the dispersion in the reference arm. The double pass loss of the free space components in sample/reference arm was ~3 dB, respectively. The back reflected power from the reference mirror and sample interfered in a 2 × 2 50/50 coupler generating two-way interferometric signal with π -phase shift after two circulators.

The interferometric signal was detected by a BD (DSC-R212, Discovery) with maximum 18-GHz 3 dB electrical bandwidth, 0.8 A/W responsivity at 1550 nm, and 3 dB low cut-off frequency at 50 kHz (typical value). The differential interference signal after the BD was digitized by a high-speed real-time oscilloscope (Lecroy SDA 820Zi-B) with 20-GHz electrical bandwidth, 80-GS/s sampling rate, and 8-bit analog-to-digital conversion resolution. The real-time oscilloscope was not only used to monitor the interference signal but also served as the signal processing and controlling center for TS-OCT. A digital-to-analog converter (DAC) card was used to control the 1D/2D scanning of the galvo mirror by the real-time oscilloscope through a USB interface. The light beam was stepwise scanned on the sample in a triangular sweep trajectory rather than a continuous mode to avoid blurring of adjacent A-scans [43]. Each scan period contained a forward and backward B-scan. All the signal processing and controlling were conducted in the built-in MATLAB platform. The signal detection, signal processing, and light beam scanning parts were synchronized through the real-time oscilloscope, while the swept source was free running for the limited signal processing speed and synchronization bandwidth for the swept source.

3. System performance

3.1 Swept source performance

The performance of the fiber laser (Fig. 2) is characterized in both spectrum and time domain with pulses directly extracted from fiber cavity. Figure 2(a) is the optical spectrum with pump power of 112 mW, which was recorded by an optical spectrum analyzer (OSA, Yokogawa AQ6375). As can be observed, it has a near-rectangle format shape with sharp rising and falling edges, and its 10-dB bandwidth is 102 nm centered at 1550 nm. The time domain pulse train was detected by a 10-GHz photodetector (PD, HP 11982A) and recorded by the real-time oscilloscope, as shown in Fig. 2(b). The pulse spacing is about 22.5 ns, consistent with the cavity length. Figure 2(c) shows the radio frequency (RF) spectrum of the output pulse train measured by an electrical spectrum analyzer (E4440A, Agilent). The resolution and span of the measurement is 1 kHz and 12 MHz for the main frame, and 10 kHz and 3 MHz for the inset. From those spectra, the laser source has fundamental repetition rate of 44.5 MHz with signal-to-noise ratio (SNR) of 80 dB, proving that this laser is stable mode-locked. Figure 2(d) is the autocorrelation trace of the mode-locked pulses directly extracted from the laser cavity through a 1.1-m pigtail of the OIM, which was measured by an autocorrelator

(Femtochrome, FR-103 MN). The full width at half maximum (FWHM) pulse width is 1.6 ps, which shows the pulses was chirped for the intracavity dispersion.

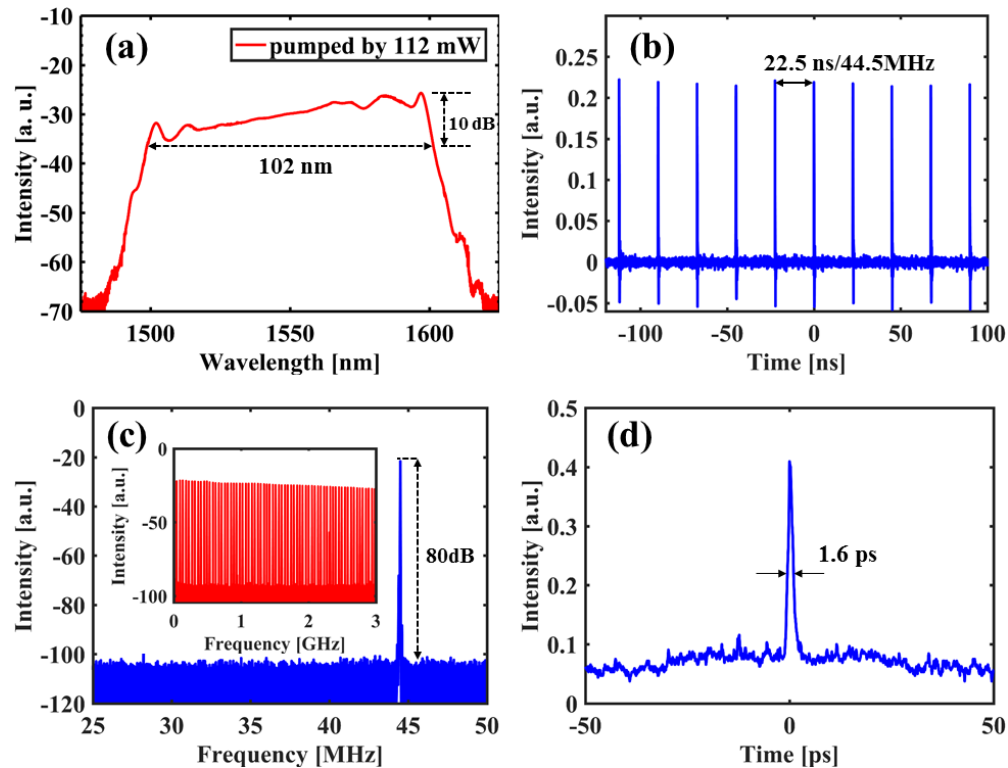


Fig. 2. Performance of the broadband mode-locked fiber laser. (a): Direct output optical spectrum; (b): Time-domain pulse train; (c): RF spectrum with 140 MHz span, and inset is 3GHz; (d): Autocorrelation trace of the mode-locked pulse.

For the time-stretch part, the optical spectrum after the SMF is shown in Fig. 3(a) in blue that has the same profile as the original spectrum (Fig. 2(a)), i.e. no fiber nonlinearity-induced distortion existed. The optical spectrum after the SOA is shown in Fig. 3(a) in red with maximum pump current of 500 mA generating 20 mW (13 dBm) output power at about 30 dB optical SNR. From these two spectrum, the short wavelength end of the spectrum experience higher gain than the longer wavelength end because the SOA has ASE peak at 1530 nm. Therefore, the SOA not only compensated the time-stretch loss, but also reshaped the slanted spectrum into a relative flattened format that increased the effective working bandwidth for OCT imaging. The time domain waveform after the SOA is shown in Fig. 3(b), which proves that the pulses was chirped into 20.6 ns corresponding to 92% duty cycle. To test the interference performance of this TS-OCT system, a mirror was used as sample, and the interference signal is shown in Fig. 3(c). Here, the DC component of the interferometric signal was completely suppressed by the BD for its low cut-off frequency. Besides, the fringes at short wavelength end is much denser than the longer wavelength side though the fringes should be a single tone for a mirror sample. Specifically, there are 10 periods in short wavelength end within 2 ns, while it is 8 periods in long wavelength side. This frequency or wavenumber (k -space) unevenly distributed (nonlinear) in time domain is induced by nonlinear frequency/wavelength to time mapping that is essentially caused by the dispersion of the SMF.

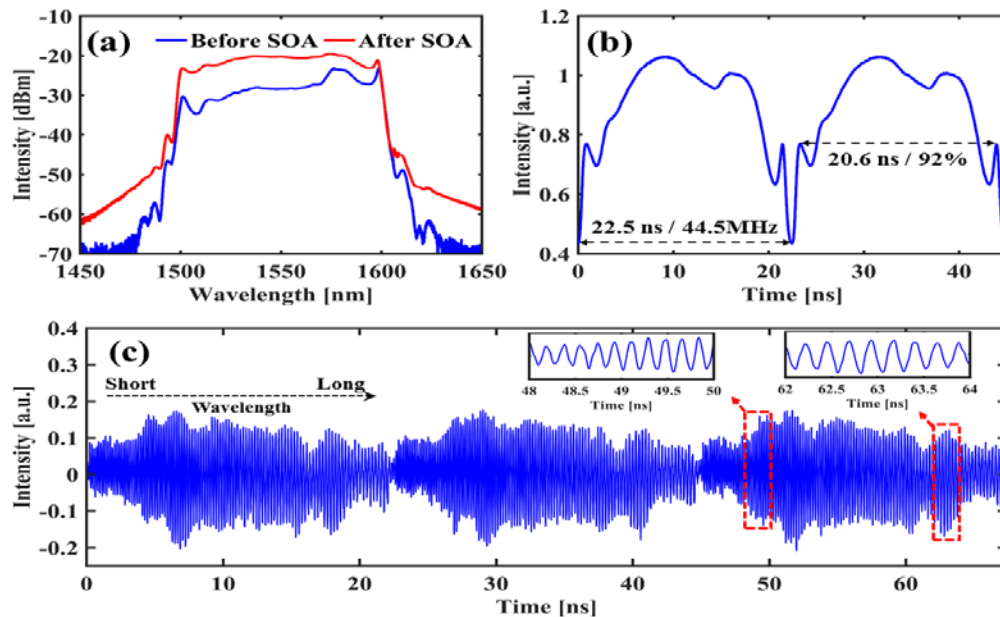


Fig. 3. (a): Optical spectrum before and after SOA, respectively; (b): Time domain waveform after SOA. (c): The real-time single-shot interferograms generated by the TS-OCT system at a repetition rate of 44.5 MHz.

3.2 k -space resampling

If fast Fourier transform (FFT) was conducted directly with this uneven/chirped sinusoidal wave, the FFT results will be distorted and thus lead to a distorted imaging eventually [22]. Therefore, a k -space resampling from uniform time to uniform wavenumber should be conducted before FFT to avoid imaging distortion.

For k -space resampling, a look-up vector that is able to remap the uneven fringes to uniform format should be found first [44,45]. For this target, the optical path length difference (OPLD) between the sample mirror and reference mirror are offset at 1 mm here, and the interference signal in one period is shown in Fig. 4(a). Hilbert transform was afterwards implemented to retrieve the phase of the fringe. By unwrapping the phase of Hilbert transform result, a look-up vector can thus be obtained for resampling purpose, as is shown in Fig. 4(b) by curve. Here, the sampling points in one period is 1602 which is determined by the duty cycle of the time-stretched pulses and sampling rate of the oscilloscope. Benefit from the stable mode-locking of the fiber laser, the pulse-to-pulse repeatability is quite high. Therefore, a single look-up vector acquired before imaging could be applied to resample all of the A-scan signal, so that the imaging and resampling parts can share the same interferometer and no calibration Mach-Zehnder interferometer (MZI) needs to be built for resampling purpose [15].

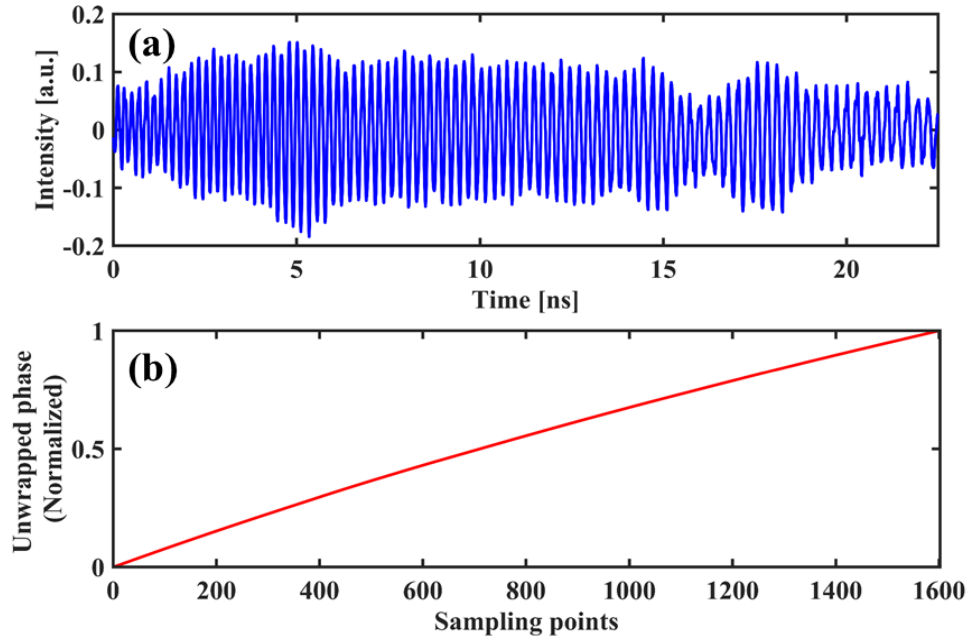


Fig. 4. (a) Interference fringe in one period with a mirror as the sample; (b) Unwrapped phase curve for sweep-by-sweep resampling.

3.3 Sensitivity roll-off and resolution

Sensitivity roll-off versus imaging depth, axial and lateral resolution are key parameters to evaluate the performance of an OCT system. Sensitivity roll-off exhibits the instantaneous linewidth of the swept source and it is determined by the electrical bandwidth and sensitivity of the BD as well. Sensitivity roll-off can be quantified by measuring the axial point spread function (PSF) at different OPLD position between the reference and sample arm, i.e. different imaging depth. A mirror was used as an axial single layer object and FFT was conducted to calculate the PSF with the interference signal after k -space resampling. Hamming window was adopted to reshape the swept waveform to minimize the side-lobe artifact of the PSF [46]. A detailed measurement method has been covered in [47]. Here, the measurement was conducted with 45 dB attenuation in the interferometer to avoid saturating the highly sensitive BD, and the measured sensitivity roll-off as a function of imaging depth of the proposed TS-OCT is shown in Fig. 5(a). The measured sensitivity of the TS-OCT system is 85 dB, and it is no obvious change at the imaging depth range from 0 to 3 mm. But beyond 3 mm, the sensitivity descends in 2.3 dB/mm. The turning point at 3 mm imaging depth is determined by the electrical bandwidth of the BD (18 GHz) and the chirped pulse width (20.6 ns). A specific analysis on the relationship between imaging range, electrical bandwidth of the receiver, and time-stretch ratio are elaborated as follows. Assuming the OPLD between the reference and sample mirror is Δz , and a BD with perfect DC suppression is used to detect the interference signal, the output of the BD, I , can be expressed as

$$I = I_{AC} \cos(2k\Delta z) = I_{AC} \cos(4\pi f_o \Delta z / c), \quad (1)$$

where I_{AC} is the amplitude of the interference fringe which is determined by the reference and sample reflectivity, source power spectral density, and responsivity of the BD. k is the free-space wave number and f_o is the optical frequency correspondingly. c is the speed of light in vacuum.

Although the interference signal is captured in time series, it is actually encoded in a broadband optical spectrum through wavelength/frequency to time mapping. When treated in optical frequency domain, the optical frequency difference, Δf , between two adjacent peaks of the interference signal can be calculated by setting $4\pi f\Delta z/c = 2n\pi$, where n is an integer. Therefore,

$$\Delta f_o = \frac{c}{2\Delta z}. \quad (2)$$

Here, the larger Δz has small Δf_o , i.e. the deeper imaging depth has denser interference fringe.

In frequency to time mapping part by dispersive fiber, assume the total GVD is x ns/nm, i.e. xc/f_o^2 ns/Hz. The time difference, Δt , between two adjacent peaks of the interference signal is

$$\Delta t = \frac{xc}{f_o^2} \Delta f_o. \quad (3)$$

When the interference signal is detected by a BD, the minimum electrical bandwidth, f_e of the BD should be,

$$f_e = \frac{1}{\Delta t} = \frac{f_o^2}{xc\Delta f_o}. \quad (4)$$

Here, larger GVD reduces the receiver bandwidth requirement.

In practice, to avoid pulse overlapping after time stretch, the maximum GVD is determined by the repetition rate and optical bandwidth of the fiber laser. In this paper, the repetition rate of the fiber laser is 44.5 MHz, and the optical bandwidth is 102 nm centered at 1550 nm (193.5 THz). The maximum GVD without pulse overlapping is 0.22 ns/nm for this laser, and 11.9-km SMF with total GVD of 0.2 ns/nm is thus used. Since 3dB electrical bandwidth f_e of the BD is 18 GHz, then $\Delta f_o = 35$ GHz is calculated by Eq. (4), and the maximum Δz is 4.3 mm by replacing $\Delta f_o = 35$ GHz into Eq. (2). The maximum Δz is the maximum OPLD, i.e. maximum imaging range. From the sensitivity roll-off curve measured in Fig. 5(a), the 3 dB sensitivity roll-off position is ~ 4.4 mm, which matches well with the calculation value.

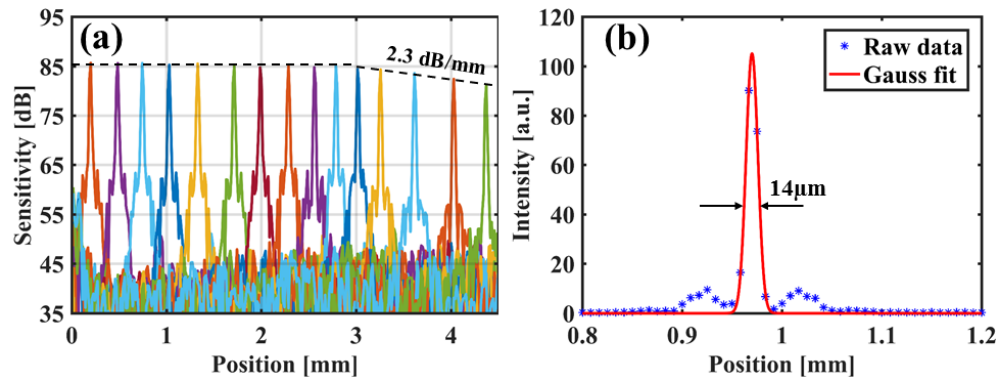


Fig. 5. (a) Sensitivity roll-off as a function of imaging depth; (b) 14 μm axial resolution in air.

The axial resolution of an OCT system can be quantified by the FWHM of the PSF, which is determined by the optical bandwidth of the swept source. By performing a Gaussian fit to the PSF, the measured axial resolution of the proposed TS-OCT is 14 μm in air corresponding to about 10 μm in tissue, as shown in Fig. 5(b). The theoretical axial resolution can be evaluated by $\Delta z = 0.44\lambda^2/\Delta\lambda$ assuming the optical source has Gaussian shape spectrum [2],

where Δz is the axial resolution, λ is the center wavelength of the swept source and $\Delta\lambda$ is its bandwidth. For the proposed TS-OCT, $\lambda = 1.55 \mu\text{m}$ and $\Delta\lambda = 0.102 \mu\text{m}$ lead $\Delta z = 10.4 \mu\text{m}$, which matches well with measurement result. The lateral resolution can be quantified with a United States Air Force (USAF) 1951 resolution target, and it is $17.5 \mu\text{m}$ in our system [48]. Lateral resolution is determined by the numerical aperture (NA) of the scanning lens through the formula of $\Delta x = 4\lambda f/(\pi d)$ [2], where Δx is the lateral resolution, λ is the center wavelength of the light source, f and d are the effective focal length and aperture size of the scanning lens, respectively.

3.4 TS-OCT imaging

In imaging, the average power illuminated on the sample was about 5 mW within the safety standard of ANSI at the conditions of continuous illumination [49]. For each scanning step, an A-scan line can be obtained after conducting k -space resampling and FFT to the interference signal. For 2D imaging, 1D scanning of a galvo mirror at either forward or backward direction is acceptable and forward scanning was used here. For 3D imaging, both forward and backward scan were used here to improve the imaging speed and they interleaved a constant distance (2 A-scan lines here) on the sample through controlling the scanning of the second galvo mirror. During the acquisition, the processing time for a single A-scan is ~ 5 ms and ~ 3 seconds for a 2D frame with 600 A-scan lines. 300 of 2D frames was saved and combined in ImageJ for 3D reconstruction [50]. The volumetric data set contains 600×300 axial scans covered $3 \text{ mm} \times 3 \text{ mm}$ imaging area on the sample. It should be noted that video-rate was not realized in current demonstration of the TS-OCT imaging, which is mainly limited by the data processing speed by current real-time oscilloscope. However, it can be ameliorated by applying high-speed data processing unit, e.g. graphics processing unit (GPU) or field-programmable gate array (FPGA) [51,52].

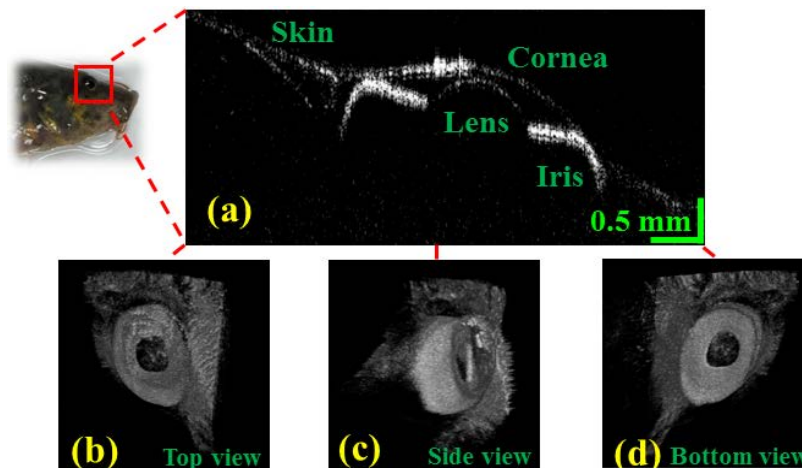


Fig. 6. (a) Cross-sectional images (2D) of an anterior segment of a mud-fish eye at center area. (b)-(d) 3D images are shown from top view, side view, and bottom view.

Figure 6 presents the images acquired with the TS-OCT system with an anterior segment of a mud-fish eye. Figure 6(a) is the 2D cross-sectional anterior segment image of the mud-fish eye at the center area. The iris is clearly shown under the cornea, and the anterior surface of the lens can be observed as well. The image shows high contrast and high penetration to the bottom of iris. Figure 6(b) to 6(d) show the 3D TS-OCT images which exhibits the anterior segment of the mud-fish eye from different perspectives with high imaging contrast. Different perspectives was realized by setting different view angle to the 3D image in ImageJ.

4. Conclusion

In summary, we report an all-fiber inertial-free swept source by incorporating a fiber mode-locked laser and time-stretch technique. The broadband high power dispersion-managed fiber laser delivers pulse train with 102-nm optical bandwidth, 22-mW average power, and 1.6-ps pulse width at 44.5-MHz repetition rate. The swept source with larger than 100 nm optical bandwidth is comparable with conventional sources based on SOA, but the repetition rate is more than two orders of magnitude higher without buffering technologies. A TS-OCT system was constructed based on this high performance swept source, which has 14 μm axial resolution in air (10 μm in tissue), flat sensitivity roll-off within 4.3 mm imaging range, and 85 dB imaging sensitivity. The 2D and 3D OCT images with a mud-fish eye anterior segment prove the imaging capability of the proposed TS-OCT system in practice. This novel swept source structure, i.e. by leveraging high performance fiber laser and time-stretch technique, provides a promising source solution for SS-OCT system to realize high-performance volumetric OCT imaging in real time.

Funding

Research Grants Council of the Hong Kong Special Administrative Region, China (Project Nos. E-HKU701/17, HKU 17205215, HKU 17208414); City University of Hong Kong (CityU T42-103/16-N); National Natural Science Foundation of China (NSFC) (N_HKU712/16); Innovation and Technology Commission (GHP/050/14GD); University Development Fund of Hong Kong University.